OPEN

A Promising Proton Conducting Electrolyte BaZr$_{1-x}$Ho$_x$O$_{3-\delta}$ (0.05 $\leq$ x $\leq$ 0.20) Ceramics for Intermediate Temperature Solid Oxide Fuel Cells

Deepash S. Saini [1*], Avijit Ghosh[2], Shuvendu Tripathy[3], Aparabal Kumar[3], Sanjeev K. Sharma[3], Nawnit Kumar[4], Shubhankar Majumdar[5] & Debasis Bhattacharya[3]

In this study, the Ho-substituted BaZrO$_3$ electrolyte ceramics (BaZr$_{1-x}$Ho$_x$O$_{3-\delta}$, 0.05 $\leq$ x $\leq$ 0.20) were synthesized through a low-cost flash pyrolysis process followed by conventional sintering. The effects of Ho-substitution in BaZrO$_3$ studied in terms of the structural phase relationship, microstructure and electrical conductivity to substantiate augmented total electrical conductivity for intermediate temperature solid oxide fuel cells (IT-SOFCs). The Rietveld refined X-ray diffraction (XRD) patterns revealed that pure phase with $Pm\bar{3}m$ space group symmetry of cubic crystal system as originated in all samples sintered at 1600 °C for 8 h. The Raman spectroscopic investigations also approved that Ho incorporation in BaZrO$_3$ ceramics. Field Emission Scanning Microscopic (FESEM) study informed a mixture of fine and coarse grains in the fracture surface of Ho-substituted BaZrO$_3$ sintered samples. The relative density and average grain size of samples were observed to decrease as per the addition of Ho-substitution in BaZrO$_3$ ceramics. The electrical conductivity study was accomplished by Electrical Impedance Spectroscopy (EIS) under 3% humidified O$_2$ atmosphere from 300 to 800 °C. Furthermore, the total electrical conductivity of BaZr$_{0.8}$Ho$_{0.2}$O$_{3-\delta}$ ceramic was found to be 5.8 $\times$ 10^{-3} S-cm^{-1} at 600 °C under 3% humidified atmosphere, which may be a promising electrolyte for IT-SOFCs.

Recently, the proton conductive oxide ceramics have fascinated worldwide attention due to widespread applications in intermediate temperature solid oxide fuel cells (IT-SOFCs), hydrogen separation and electrolysis of steam, etc. In this context, the rare-earth cerates and zirconates with the perovskite-type A(II)B(IV)O$_3$ crystallographic structure are the two foremost families of proton-conducting oxides for electrochemical applications[1-4]. Generally, in these categories of oxide materials, oxygen vacancies are increased by replacement of tetravalent cation B(IV) by trivalent cation M(III) as given in the Eq. (1) using Kröger-Vink notation.

$$2B_B^x + O_O^x + M_2O_3 \rightarrow 2M'_B + V_O^{\bullet\bullet} + 2BO_2 \qquad (1)$$
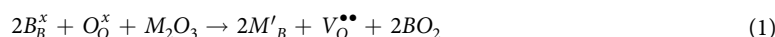
In this case, an H$_2$O molecule from the vapor phase dissociates into hydroxide (OH^-) ion and proton (H^+) in these oxide materials. The hydroxide (OH^-) ion fills up an oxygen vacancy, and proton (H^+) forms a hydroxide (OH^-) ion with oxygen lattice[5-7] according to the Eq. (2).

$$H_2O(g) + V_O^{\bullet\bullet} + O_O^x \rightarrow 2OH_O^- \qquad (2)$$

The protons are induced in these types of the perovskite oxides through oxygen vacancies due to replacement of tetravalent cation B(IV) by trivalent cation M(III). This proton conducts through hopping to the adjacent oxygen site and revolving around the oxygen that contribute to the protonic conductivity in the material[6,7]. Furthermore, trivalent cation M(III) substituted barium zirconates (i.e. BaZr$_{1-x}$M$_x$O$_{3-\delta}$) are more chemically

¹Department of Physics, Deen Dayal Upadhaya Gorakhpur University, Gorakhpur, 273009, India. ²Department of Physics, Central University of Jharkhand, Ranchi, 835205, India. ³Materials Science Centre, Indian Institute of Technology, Kharagpur, 721302, India. ⁴Department of Physics, Malti Dhari College, Naubatpur, Patliputra University, Patna, 801109, India. ⁵Department of Electronics and Communication Engineering, National Institute of Technology, Meghalaya, 793003, India. *email: dssainiddugu@gmail.com

stable than the typical proton-conducting barium cerate and have decent proton conductive activity under a wet atmosphere[8,9].

Furthermore, the trivalent cation substituted $BaZrO_3$ powders are generally synthesized by the solid-state reaction method through oxide or carbonate precursors. In addition to that, several wet chemical methods have also been employed to prepare the above powders, such as co-precipitation[10], modified Pechini[11], glycine-nitrate[12,13], sol-gel[14,15], polyacrylamide gel[16], molten salt[17,18], and hydrothermal methods[19,20], etc. All these ways, contemporary afford their merits and demerits. In the sol-gel process, the rate of hydrolysis of different types of metal alkoxide limits its usage, while, inhomogeneity in compositional distribution and agglomeration of particles are the main bottlenecks in co-precipitation method[21]. Furthermore, inhomogeneous particle size, as well as irregular morphology in hydrothermal route, restricts the use of this process. An alternative way, a high temperature ($>1400\,°C$) is required to synthesize single-phase material considerable a large size ($>100\,nm$) of particle. However, the oxide nano-particles are desirable for good sinterability with large grain size and reflect high conductivity of perovskite material[22]. Therefore, from the perspective of synthesis, it is still an open challenge to prepare the oxide nano-particles at a relatively low temperature.

Other than the above, the substitution of a trivalent cation is recurrently exploited to escalation the conductivity of zirconates. The numerous factors, such as electronegativity, ionic radius, and so on, should be considered in a sophisticated way of choosing the substituent[23,24]. Trivalent elements include rare-earth elements, transition elements, and several main groups of elements, such as Y^{3+}, Gd^{3+}, Yb^{3+}, Dy^{3+}, Sm^{3+}, In^{3+}, Sc^{3+}, etc[25,26]. are typically used as a substituent for zirconates. Recent theoretical investigations have revealed that the ionic radius of substituent directly controls substituent-proton interaction energy. Furthermore, the ionic radius of substituent directly controls the trapping effect of protons by a substituent, also. The trapping effect of protons by substituent is minimum for Y ($90\,pm$) substituted $BaZrO_3$ ceramics[23,24]. In this context, Y-substituted $BaZrO_3$ ceramics have engrossed prodigious attention because of its effective proton conductivity and many researchers are also working on it[9,27,28]. But, some researcher reported very little proton conductivity for trivalent substituted $BaZrO_3$[9,27–30]. However, Kreuer et al.[30] demonstrated that single crystal of Y-substituted $BaZrO_3$ had reasonably high proton conductivity ($5 \times 10^{-5}\,S\text{-}cm^{-1}$) even at 140 °C. Then Bohn and Schober[9] established the enormous proton bulk conductivity ($3 \times 10^{-3}\,S\text{-}cm^{-1}$) of it in a wet hydrogen atmosphere at 600 °C. Furthermore, Han et al. reported a remarkably large conductivity of Dy-substituted $BaZrO_3$ under humidified reducing environment, which is reduced unusually under oxidizing atmosphere because of instability in oxidization state of Dy from 3+ to 4+ state[31]. Similarly, Ahmed et al. presented total conductivity of $1 \times 10^{-4}\,S\text{-}cm^{-1}$ for Yb-substituted $BaZrO_3$ at 600 °C under wet air[32] and also conductivity of $1 \times 10^{-4}\,S\text{-}cm^{-1}$ for hydrated In-substituted $BaZrO_3$ at 600 °C[33]. But, according to theoretical studies, the Ho-substituted $BaZrO_3$ may support to progress the conductivity and explore the new substituent for $BaZrO_3$ regarding proton-conducting electrolyte since the ionic radius of Ho^{3+} ($90.1\,pm$) is very similar to that of Y^{3+} ($90\,pm$)[34]. However, the study about Ho-substituted $BaZrO_3$ has been little consideration in the scientific world so far[34–36]. In this work, we adopted Ho as a single substituent for $BaZrO_3$ ceramics to explore the influence of Ho^{3+} on the electrical properties of $BaZrO_3$ ceramics for operative SOFC applications.

Results and Discussion

Structural and microstructural behaviours of $BaZr_{1-x}Ho_xO_{3-\delta}$ ($0.05 \leq x \leq 0.20$).

The structural phase investigation of calcined powders and sintered pellets of Ho-substituted $BaZrO_3$ were carried out using XRD technique, and their XRD patterns are presented in Figure 1(a–d). The XRD patterns of all Ho-substituted samples calcined at 1100 °C exhibit no impurity phase. The consequences of XRD are consistent with the corresponding DTA-TGA results, where negligible mass loss is observed above 1100 °C (Figure S1). Furthermore, assuming a cubic crystal system with $Pm\bar{3}m$ space group in all the Ho-substituted samples calcined at 1100 °C and sintered at 1600 °C, we have completed the Rietveld refinements of these XRD patterns. Hence, the refined patterns are made as a solid line in the respective Figure 1(a–d)[37]. The distinguished structural parameters are tabulated in Table S1.

Analyzing all XRD patterns, it is manifested that flash pyrolysis process is very effective to prepare the pure phase of Ho-substituted $BaZrO_3$ ceramics. The lattice parameter (Table S1), unit cell volume, Zr/Ho-O and Ba-O bond lengths are increased with substitution of Ho^{3+} in $BaZrO_3$. This is in accordance with high ionic radius of Ho^{3+} ($\sim90.1\,pm$) compare to Zr^{4+} ($\sim72\,pm$). Furthermore, the crystallinity of all samples is decreased with the increase of Ho substitution in $BaZrO_3$ samples (Table S1) may be due to lower diffusion rates of the cation with an increase of Ho-substitution in $BaZrO_3$. The unit cell parameters extract from XRD patterns through Rietveld refinement method corresponding to $x = 0.05$, 0.10, 0.15 and 0.20 for $BaZr_{1-x}Ho_xO_{3-\delta}$ samples afterward sintered at 1600 °C were 4.1972, 4.1992, 4.2034 and 4.2057 $A°$, respectively. Therefore, it can be conjectured that the amount of Ho was completely incorporated at Zr-site of $BaZrO_3$ perovskite, and its effective negative charge is completely counterbalanced by oxygen vacancies. The corresponding shift in the XRD peaks in the direction of the lower diffraction angles with the increase of Ho-substitution representing an increment of volume of the unit cell is apparent from Figure S2, also.

The microstructural investigation was carried out using HRTEM study. The Figue 2(i–iv) displays (a) a typical bright field HRTEM image, (b) corresponding selected area electron diffraction (SAED) pattern, (c) lattice plane, and (d) simulated lattice plane for $BaZr_{1-x}Ho_xO_{3-\delta}$ ($x = 0.05$, 0.10, 0.15, and 0.20) nano-particles calcined at 1100 °C for 4 h, respectively. The HRTEM images of $BaZr_{1-x}Ho_xO_{3-\delta}$ ($x = 0.05$, 0.10, 0.15, and 0.20) samples reveal that particles are in sub-micrometer aggregation of nanocrystallites. The shape and size of particles are changed as substitution of Ho in $BaZrO_3$ ceramics increases. The proof of crystal symmetry of $BaZr_{1-x}Ho_xO_{3-\delta}$ ($x = 0.05$, 0.10, 0.15, and 0.20) nano-particles was provided by using the SAED pattern as shown in Figure 2{i(b)–iv(b)}. In this figure, rings with spots are a well-known sign of the polycrystalline nature of all Ho-substituted $BaZrO_3$ samples. It can be indexed with the plane of pure cubic crystal system for $Pm\bar{3}m$ space group. The orientation of the
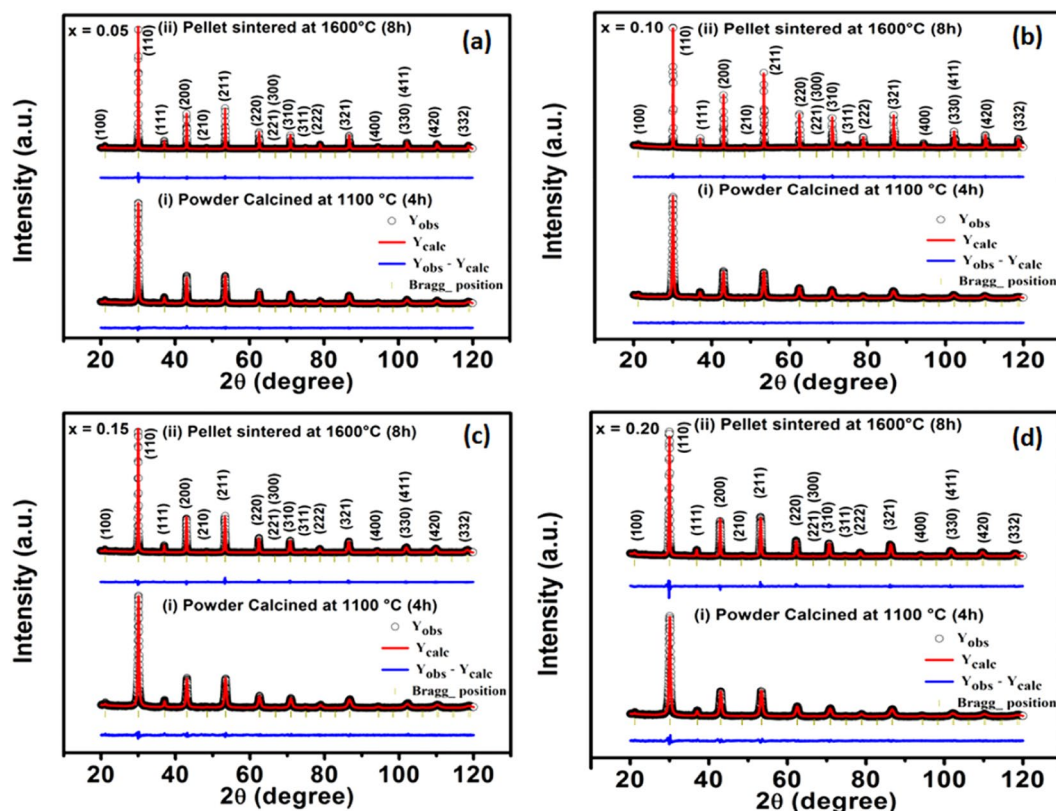
Figure 1. Rietveld refined XRD patterns of $BaZr_{1-x}Ho_xO_{3-\delta}$ ceramics for (**a**) $x = 0.05$, (**b**) 0.10, (**c**) 0.15, and (**d**) 0.20 calcined at (i) 1100 °C for 4 h and sintered at (ii) 1600 °C for 8 h.

lattice plane remains established using simulated lattice pattern of square lattice plane image, as shown in Figure 2{i(d)–iv(d)}. The difference between two consecutive peaks confirms the lattice plane spacing (d_{hkl}). The lattice plane spacing (d_{hkl}) of all samples calculated from the simulated lattice pattern is comparable with lattice plane spacing (d_{hkl}) estimated from the XRD pattern of all respective samples, as shown in Table 1.

Figure 3(a–d) exhibits the FESEM images of fracture surface for a pellet of $BaZr_{1-x}Ho_xO_{3-\delta}$ ($x = 0.05, 0.10, 0.15$, and 0.20) samples sintered at 1600 °C for 8 h in air. The FESEM images exhibit that bimodal type of grains in all the samples except for $x = 0.20$. Furthermore, the average grain size is decreased with the increase of Ho-substitution in $BaZrO_3$, as displayed in Table 2 (Figure S3). Therefore, a decrease in average grain size recommends the lower diffusion rates of the cation with an increment of Ho-substitution in $BaZrO_3$[38,39].

All the sintered pellets at 1600 °C for 8 h have relative densities of >91%, as shown in Table 2. The Ho-substituted $BaZrO_3$ sintered samples at 1600 °C for 8 h have microstructural mixtures of coarse and fine grains, as shown in Figure S3 (Table 2) through the grain size distribution curve. The microstructures of Ho-substituted $BaZrO_3$ samples are same as that of Y-substituted $BaZrO_3$ due to comparable ionic radius (Ho = 90.1 pm and Y = 90 pm), whose microstructure is the combination of fine and coarse grains as reported earlier[34]. This type of microstructure is due to the mixture of the different phases at a particular condition of synthesis and sintering temperature. The mixture of different phases reveals that cations should diffuse over a large distance to achieve equilibrium phase at 1600 °C, while the sintering time for 8 h is not sufficient for sintering to achieve equilibrium phase at 1600 °C[38]. However, there is no evidence in appearance of two phases in XRD patterns of Ho-substituted $BaZrO_3$ ceramics calcined at 1100 °C for 4 h.

Raman studies. Figure 4 exhibits Raman scattering spectra of $BaZr_{1-x}Ho_xO_{3-\delta}$ ($x = 0, 0.05, 0.10, 0.15$, and 0.20) ceramics sintered at 1600 °C for 8 h in air from 100 to 1000 cm^{-1} range. Generally, it is expected that Raman spectrum of ideal perovskite structure is featureless. But, there are several vibrational modes observed in all the samples. As there could be neither oxygen vacancies nor substituent atoms in $BaZrO_3$, so it is expected that all observed active vibrational modes are only due to second-order scattering[40,41]. However, Karlsson et al.[42] reported that vibrational mode around 200 cm^{-1} is associated with the torsional motion of lattice, which originates due to lattice distortion. Furthermore, Slodczyk et al.[42] suggested that vibrational modes in Raman spectrum of $BaZrO_3$ are mainly attributed to nanodomains having local symmetry different from that of cubic symmetry. As this spectrum consists of a broad band, so it is expected that distortions in cubic lattice to be small. In all samples, most of the bands exhibit some shifting and different intensity with the variation of composition. The appearance up of translation oscillation modes from 50 to 250 cm^{-1} is promoted by the motion of Ba^{2+} in the BaO_{12} cuboctahedra networks, which is dominated by Coulombic interactions[42–44]. At high frequencies, the peaks are mainly attributed to the mode of strongly covalent bonded oxygen in ZrO_6 octahedral networks[40–42]. Therefore, the peaks
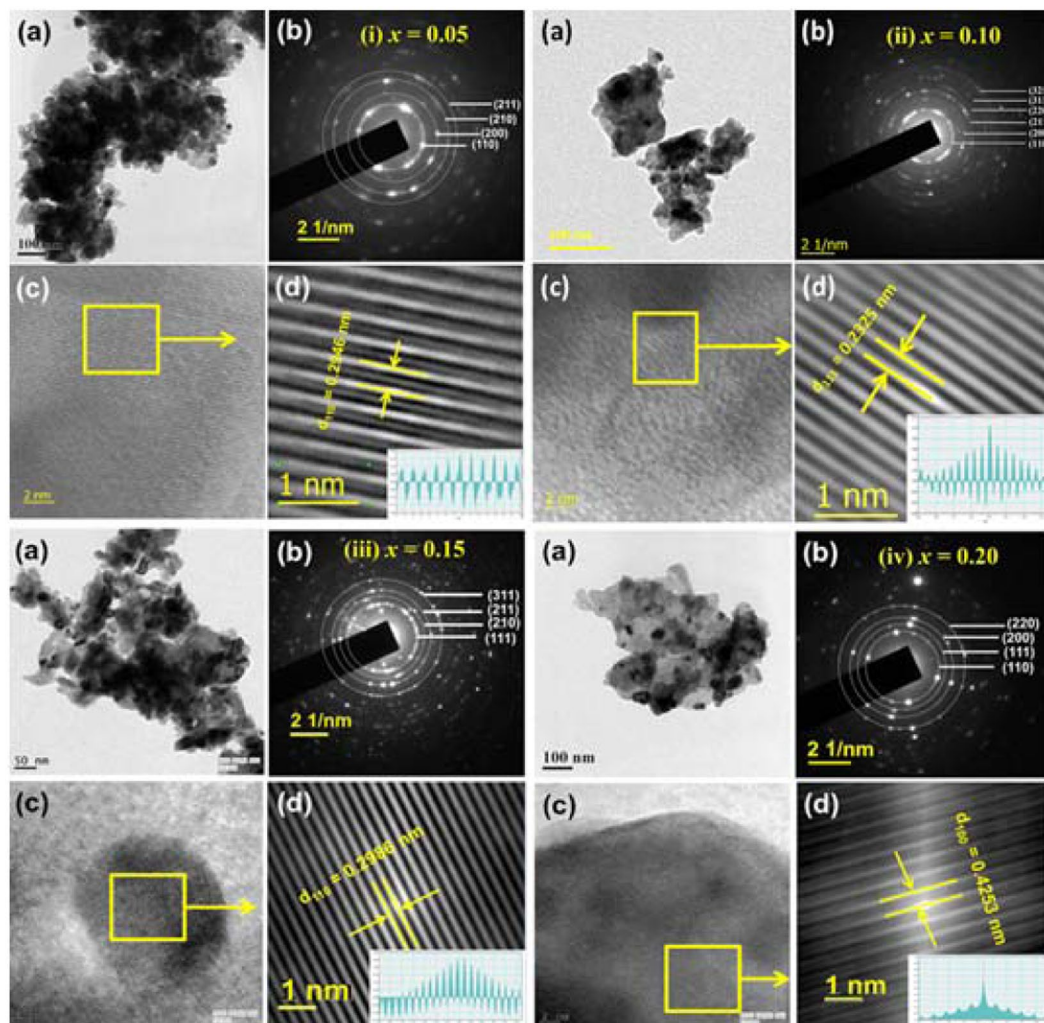
Figure 2. (**a**) A typical bright field TEM image, (**b**) corresponding selected area electron diffraction pattern (SAED), (**c**) lattice plane and (**d**) the simulated lattice plane of $BaZr_{1-x}Ho_xO_{3-\delta}$ ceramic nano-particles for (i) $x = 0.05$, (ii) 0.10, (iii) 0.15, and (iv) 0.20 calcined at $1100\,°C$ for $4\,h$.

| x	Lattice constant obtained from XRD Pattern (*nm*)	Lattice plane (*hkl*)	Lattice planar spacing (d_{hkl}) obtained from XRD pattern (*nm*)	Lattice planar spacing (d_{hkl}) obtained from SAED pattern (*nm*)
0.05	4.1981	110	0.2958	0.2946
0.10	4.2021	111	0.2326	0.2345
0.15	4.2052	110	0.2971	0.2988
0.20	4.2068	100	0.4233	0.4253

Table 1. A comparison of the lattice planar spacing (d_{hkl}) obtained from XRD and SAED pattern of $BaZr_{1-x}Ho_xO_{3-\delta}$ ceramics for $x = 0.05$, 0.10, 0.15, and 0.20 calcined at $1100\,°C$ for $4\,h$ in air.

from 300 to 500 cm^{-1} and 600 to 900 cm^{-1} range can be due to bending (*d*) and symmetric stretching (*n*) modes of oxygen bonds, more specially[43,44].

In case of Ho-substituted $BaZrO_3$ ceramics ($x = 0.05$, 0.10, 0.15 and 0.20), the vibrational band from 250 to 900 cm^{-1} range is associated to distortion of Zr/HoO_6 octahedra because of tilting of Zr/HoO_6 octahedra and a slight distortion of Zr/HoO_6 in the direction of c-axis. This distortion in octahedra is mainly due to accommodation of larger size of Ho^{3+} atom (90.1 *pm*) at Zr-site (72 *pm*) and formation of oxygen vacancies in $BaZrO_3$[41–44]. The weak vibration band around 130 cm^{-1} is assigned to deformational motion and stretching vibrations of $Ba-Zr/HoO_6$[41]. This band is the signature of structure of Ho-substituted $BaZrO_3$ perovskite and indicates a cubic structure of perovskite without any structural phase transition[42]. The vibration bands from 200 to 900 cm^{-1} range become more intense and broad as substituent concentration in $BaZrO_3$ increases. It reveals that local deformations become more pronounced without changing the inclusive feature of spectra as Ho-concentration increases.

x	Average grain size (μm)		Relative density (%)
	Small grain	Large grain	
0.05	0.43	1.18	94.7
0.10	0.34	1.04	93.5
0.15	0.26	0.82	92.6
0.20	—	0.73	91.3

Table 2. Average grain size from facture surface and relative density of $BaZr_{1-x}Ho_xO_{3-\delta}$ ceramics for $x = 0.05$, 0.10, 0.15, and 0.20 sintered at 1600 °C for 8 h in air.
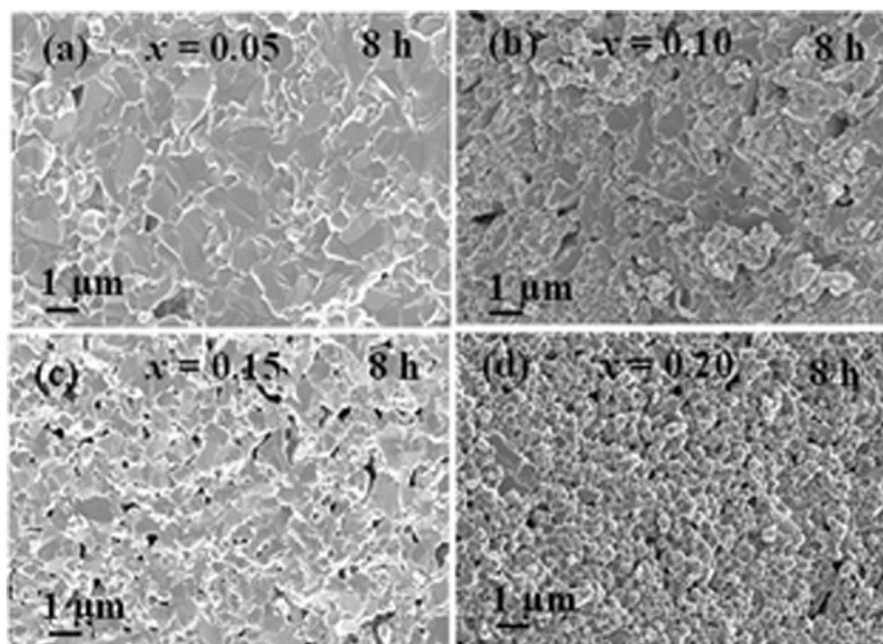

Figure 3. FESEM micrographs from fracture surface of $BaZr_{1-x}Ho_xO_{3-\delta}$ ceramics for (**a**) $x = 0.05$, (**b**) 0.10, (**c**) 0.15, and (**d**) 0.20 sintered at 1600 °C for 8 h in air, respectively.
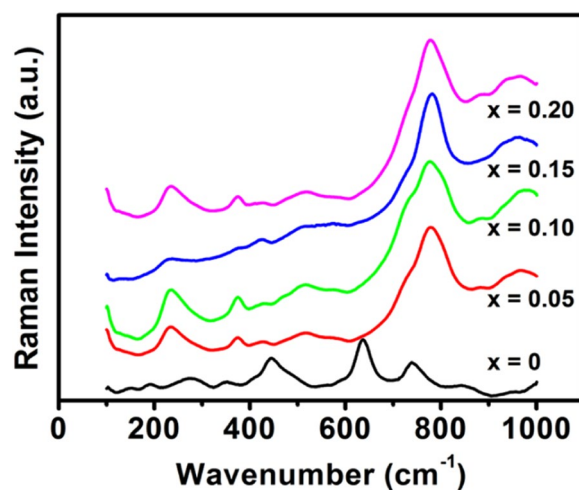
Figure 4. Raman spectra of $BaZr_{1-x}Ho_xO_{3-\delta}$ ceramics for $x = 0$, 0.05, 0.10, 0.15, and 0.20 sintered at 1600 °C for 8 h in air, respectively.

The long-range average cubic structure remains similar as observed in XRD patterns. The distortion in the perovskite structure of pure and Ho-substituted $BaZrO_3$ ceramics are completely diverse from each other. It can be identified by the shift of mode near 250 to 350 cm^{-1} towards the lower wave number for $x = 0$ to $x = 0.20$ substituent content and established to change in the tilt angle of ZrO_6 octahedra[45].
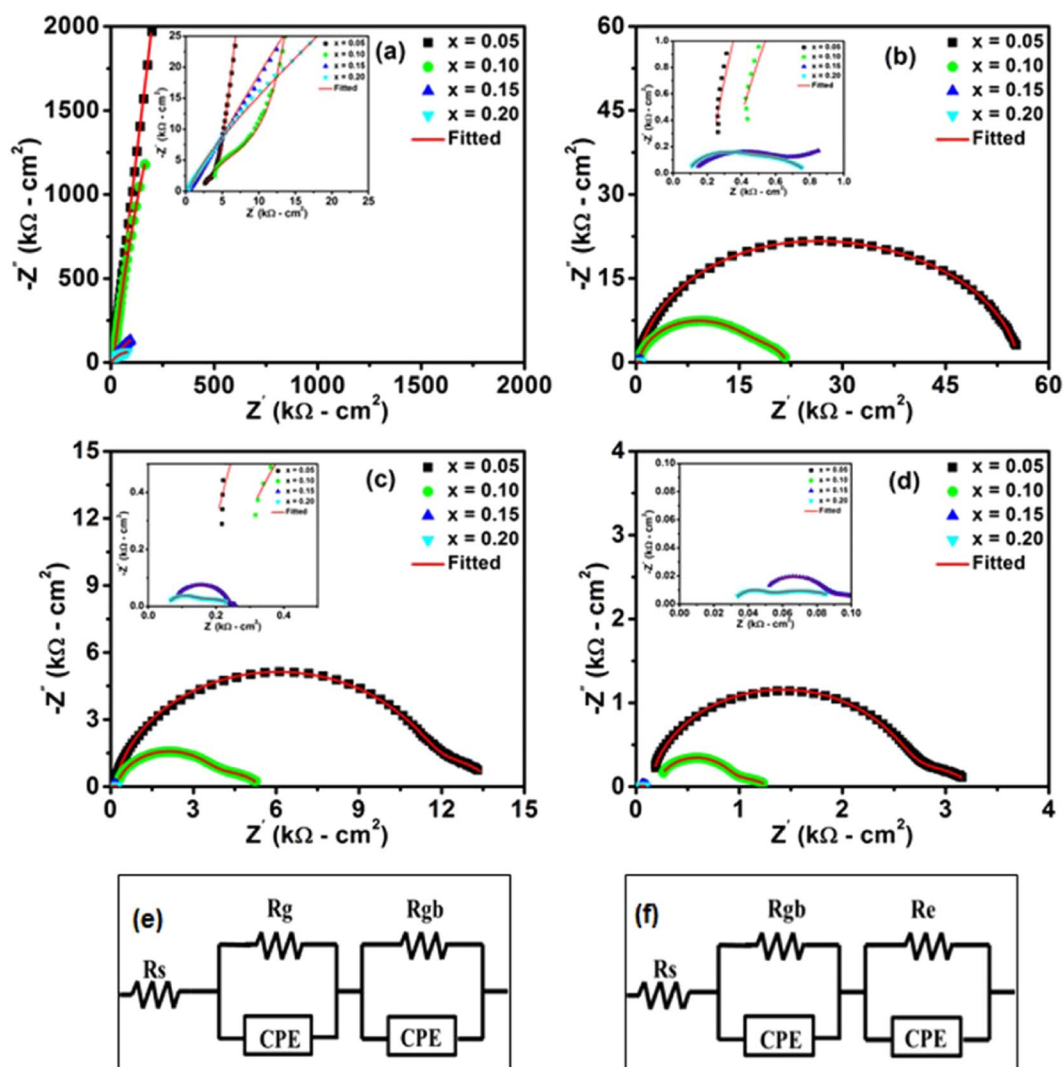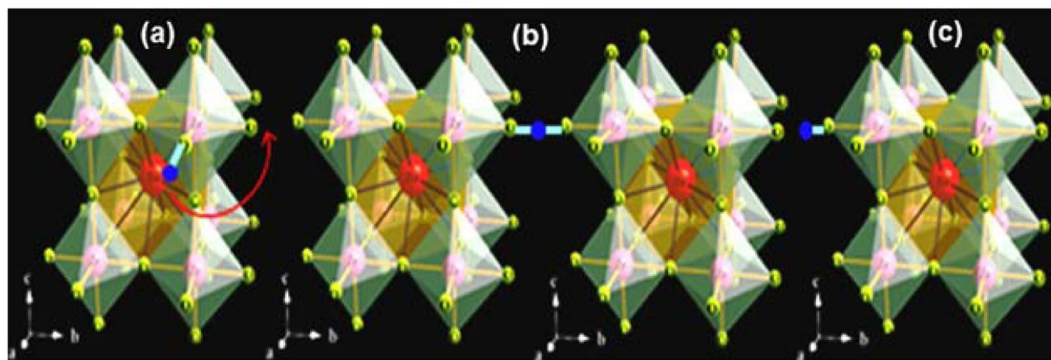
Figure 5. Complex impedance spectra (Nyquist plots) of BaZr$_{1-x}$Ho$_x$O$_{3-\delta}$ ceramics for $x =$ 0.05, 0.10, 0.15 and 0.20 at (**a**) 300 °C, (**b**) 600 °C, (**c**) 700 °C, and (**d**) 800 °C in 3% humidified O$_2$ atmosphere, respectively. Electrical equivalent circuits used to fit impedance data of Ho-substituted BaZrO$_3$ samples, (**e**) circuit fits the impedance data at 300 °C and (**f**) circuit fits the impedance data at 600, 700, and 800 °C, respectively.

Electrical impedance analysis. The impedance spectra (Nyquist plots) of BaZr$_{(1-x)}$Ho$_x$O$_{3-\delta}$ ($x = 0.05, 0.10,$ 0.15, and 0.20) ceramics in 3% humidified O$_2$ atmosphere at 300, 600, 700, and 800 °C, respectively are offered in Figure 5(a–d), where equivalent electric circuit are employed for the analysis of impedance data. For calculation of resistance, the ZSimpWin 3.21 software is exploited for impedance spectra fitting and corresponding equivalent electric circuit is displayed in Figure 5(e,f). Out of the two circuits shown, the circuit displayed in Figure 5(e) fits the data at 300 °C temperature, meanwhile the circuit in Figure 5(f) fits the data at 600, 700, and 800 °C temperature, respectively. In these electric circuits, R_g, R_{gb} and R_e signify the grain (bulk), grain-boundary and electrode resistance, respectively. Furthermore, the R_s and CPE characterize series resistance and constant phase element, respectively.

The complex impedance spectra from Nyquist plots for all samples at 300 °C in 3% humidified O$_2$ atmosphere exhibits the existence of two depressed semicircular arcs. It reveals that two types of relaxation phenomena with sufficiently different relaxation times occurred in the materials at 300 °C. The low resistive arc at high frequency regime and high resistive arc at low frequency region are attributed to contribution from grain (bulk) interior and grain boundary, respectively. Furthermore, complex impedance spectra for all samples at 600, 700 and 800 °C exhibit again two depressed semicircles. However, the meanings of semicircular arcs are unlike from complex impedance spectra at 300 °C. The semicircle at high frequency side is possibly due to contribution from grain boundary and semicircle at low frequency side may be attributed to electrode polarization[46]. Furthermore, the capacitance value associated with bulk interior, grain boundary, and electrode polarization is found to around 10^{-11}, 10^{-9}, and 10^{-6} F, respectively[27]. The shape of semicircular arcs differs with respect to Ho-content and temperature, while the radii of these semicircular arcs decrease as such Ho-content and temperature increase. This observation exhibits the variation in resistive and capacitive part of the material. At high temperature, the

Figure 6. Schematic representation of the Grotthus mechanism for proton conduction.

contribution from grain in complex impedance spectra for all samples disappears. This may be attributed to high values of bulk relaxation frequency, preventing the appearance of arc at high temperature[47,48]. Thus, grain boundary effect dominates in all samples at high temperatures[49–51].

The total electrical conductivity of Ho-substituted BaZrO$_3$ ceramics.　It is considered from the past few years that there would be promising solid oxide fuel cell applications if advanced intermediate temperature proton conductors would be built up. In this context, the total electrical conductivity of Ho-substituted BaZrO$_3$ has been attempted in 3% humidified atmosphere. The Ho-substitution on Zr-site in BaZrO$_3$ promotes to form an oxide ion vacancy as provided in Eq. (3) through Kröger-Vink notation.

$$2Zr_{Zr}^x + O_O^x + Ho_2O_3 \rightarrow 2Ho'_{Zr} + V_O^{\bullet\bullet} + 2ZrO_2 \qquad (3)$$
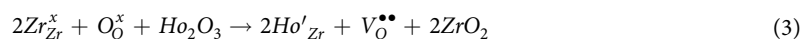
The water molecule from vapor phase split up into OH^- and H^+ ions. The OH^- ion fills up an oxide ion vacancy, and the H^+ helps to form an OH^- ion with oxygen lattice as specified in Eq. (2). As a result, the protons are induced by filling oxygen vacancies created by the substitution of the trivalent cation (Ho) into Zr site in BaZrO$_3$ ceramics from 300 to 600 °C ranges. Thus, the conducting species may be proton (H^+), oxide ion vacancy and hole in wet conditions[52], which depends upon the gas atmosphere, and temperature, etc. Furthermore, the conduction of proton in such materials takes place according to the Grotthus mechanism. In this mechanism, proton conduct through a diffusion process, which is the combination of molecular reorientation around oxygen and the hopping of proton from oxygen to nearest neighbour oxygen (Figure 6)[53,54].

The total electrical conductivities were deduced in terms of resistance determined from the impedance data through accounting for sample geometry according to Eq. (4).

$$\sigma = \frac{L}{A}\left(\frac{1}{Rg + Rgb}\right) \qquad (4)$$

where, L is the sample thickness, A is area, R_g and R_{gb} are grain (bulk) and grain boundary resistance, respectively. At higher temperature, the semi-circular arc due to grain (bulk) interior and grain boundary cannot be clearly resolved. Therefore, the total resistance of the material can be calculated from intermediate frequency intercept of complex impedance spectra (corresponding to contribution from grain boundary) with the real axis at high temperature region. Furthermore, the total electrical conductivity of BaZr$_{1-x}$Ho$_x$O$_{3-\delta}$ ($x = 0.05$, 0.10, 0.15, and 0.20) samples in 3% humidified O$_2$ atmospheres is shown in Figure 7. The BaZr$_{1-x}$Ho$_x$O$_{3-\delta}$ sample for $x = 0.20$ exhibits highest total electrical conductivity in 3% humidified atmosphere as revealed in Figure 7. Table 3 presents a detailed comparison between conductivities obtained under the present study and previous reports.

In general, the wet atmosphere boosts up the total electrical conductivity of the material significantly at the temperature region of 300 to 600 °C and oxygen partial pressure[55,56]. The overall electrical conductivity of the material also depends upon several factors such as charge carrier concentration, nature of moving charge carrier, mobility of charge carrier, etc. In 3% humidified O$_2$ atmosphere, the hydration of BaZr$_{(1-x)}$Ho$_x$O$_{3-\delta}$ ($x = 0.05$, 0.10, 0.15, and 0.20) lattice by H$_2$O molecules lead to remarkable proton conductivity, as shown through Eq. (2). At low temperatures (<600 °C), the reaction equilibrium presented by Eq. (2), is most favourable for proton formation. This signposts that the total conductivity may be dominated by conduction of proton in the samples. The total electrical conductivity in 3% humidified O$_2$ atmosphere is increased with the addition of amount of Ho-content throughout the temperature ranges (Figure 7). An increase in the total electrical conductivity may be due to proton, which is the majority charge carrier in 3% humidified O$_2$ atmosphere and increased with the increase of Ho-concentration. Furthermore, ionic radius of Ho^{3+} (90.1 pm) is larger than that of Zr^{4+} (72 pm), which expands the unit cell of BaZrO$_3$ and volume of the unit cell with the increasing amount of Ho-content in BaZrO$_3$ ceramics. This leads to enhance the width of migration channel for proton conduction. The grain boundary conductivity is dominating (Nyquist plots) in a wet oxidizing atmosphere at all elevated temperature because of core-space charge layer in the grain boundary, which give rise to the depletion of positive charge in the layer near to boundary core[57]. Furthermore, the activation energy for all samples is higher than 1 eV under
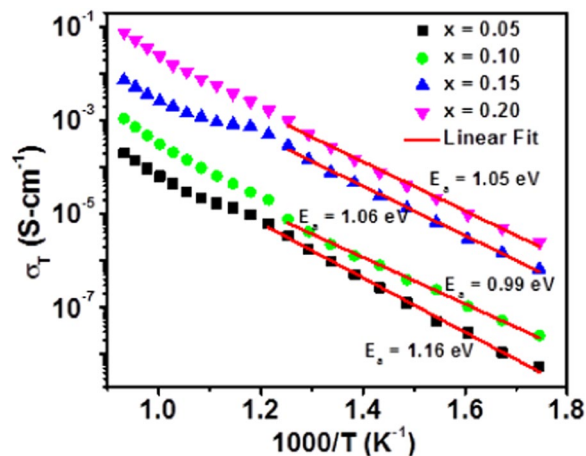
Figure 7. The total electrical conductivity of BaZr$_{1-x}$Ho$_x$O$_{3-\delta}$ ceramics for $x = 0.05$, 0.10, 0.15, and 0.20 in 3% humidified O$_2$ atmospheres.

M	Ionic radius (*pm*)	*x*	Conductivity (*S-cm^{-1}*)	Activation energy (*eV*)	Sintering conditions	Measurement conditions	Ref.
Sc	74.5	0.20	2.90×10^{-4} at 500 °C	0.98	1600 °C/8 h in air	Humidified atmosphere	[26]
In	80.0	0.20	6.90×10^{-4} at 600 °C	0.89	1600 °C/8 h in air	Humidified atmosphere	[26]
		0.75	1.00×10^{-4} at 600 °C	0.81	1325 °C/48 h in air	Dry Ar atmosphere	[33]
Lu	86.0	0.20	2.80×10^{-5} at 400 °C	0.90	1600 °C/8 h in air	Humidified atmosphere	[26]
Yb	86.8	0.20	1.10×10^{-2} at 600 °C	—	1600 °C/24 h in O$_2$	5% H$_2$O – H$_2$ atmosphere	[58]
		0.10	5.60×10^{-5} at 550 °C	—	1500 °C/48 h in air	Dry air	[32]
Tm	88.0	0.20	1.13×10^{-2} at 600 °C	—	1600 °C/24 h in O$_2$	5% H$_2$O – H$_2$ atmosphere	[58]
Er	89.0	0.20	1.36×10^{-2} at 600 °C	—	1600 °C/24 h in O$_2$	5% H$_2$O – H$_2$ atmosphere	[58]
Y	90.0	0.20	5.80×10^{-4} at 550 °C	0.86	1600 °C/8 h in air	Humidified atmosphere	[26]
		0.20	2.29×10^{-2} at 600 °C	—	1600 °C/24 h in air	H$_2$O saturated N$_2$ atmosphere	[39]
		0.20	1.39×10^{-2} at 600 °C	—	1600 °C/24 h in O$_2$	5% H$_2$O – H$_2$ atmosphere	[58]
Ho	90.1	0.05	2.96×10^{-5} at 650 °C	1.16	1600 °C/8 h in air	3% humidified O$_2$ atmosphere	Present work
		0.10	1.42×10^{-4} at 650 °C	0.99			
		0.15	1.43×10^{-3} at 650 °C	1.06			
		0.20	1.11×10^{-2} at 650 °C	1.05			
Gd	93.8	0.20	1.80×10^{-4} at 600 °C	0.74	1600 °C/8 h in air	Humidified atmosphere	[26]
Sm	95.8	0.20	8.90×10^{-5} at 600 °C	0.96	1600 °C/8 h in air	Humidified atmosphere	[26]
Nd	98.3	0.07	2.01×10^{-5} at 628 °C	—	1700 °C/1 h in vacuum	Humid air	[59]

Table 3. Comparison of the total electrical conductivity for BaZr$_{1-x}$M$_x$O$_{3-\delta}$ (M = Sc, In, Lu, Yb, Tm, Er, Y, Ho, Gd, Sm and Nd) proton-conducting electrolyte ceramics.

3% humidified O$_2$ atmosphere. However, the activation energy is higher than typically observed for proton conduction in Y-substituted BaZrO$_3$ ceramics (typically 0.45–0.55 *eV*). This discrepancy may be attributed to partial hydration of samples in 3% humidified O$_2$ atmosphere and the total electrical conductivity is probably mainly due to the conduction of both proton and oxygen vacancy. The total electrical conductivity obtained in such an environment is 5.8×10^{-3} S-cm^{-1} at 600 °C for BaZr$_{0.8}$Ho$_{0.2}$O$_{3-\delta}$. This is almost the same order to that of Y, Yb, Tm, Er, Ho-substituted BaZrO$_3$ ceramics sintered at 1600 °C for 24 h as accessible in Table 3. Furthermore, the total conductivity of BaZr$_{0.8}$Ho$_{0.2}$O$_{3-\delta}$ sample is one or two orders greater than that of Sc, In, Lu, Y, Gd, and Sm-substituted BaZrO$_3$ ceramics sintered at 1600 °C for 8 h[26,32,33,38,58,59]. The variation of the total electrical conductivity with the concentration of Ho-substitution is revealed in Figure S4. The total electrical conductivity measured at 600 °C for $x = 0.20$ is nearly three orders higher than that for $x = 0.05$ concentration. At higher temperature (>600 °C), the slope of Arrhenius plot changes in the conductivity plots. This indicates that the conductivity is attributable to conduction of hole or oxide ion, and not for the conduction of proton. Bohn and Schober have also stated similar findings for Y-doped BaZrO$_3$ perovskites[9]. However, an increase in the total conductivity at higher temperatures, under O$_2$ environment settles that hole conduction is dominating, according to the following reaction:

$$1/2O_2(g) + V_O^{\bullet\bullet} \leftrightarrow O_O^x + 2h^\bullet \tag{5}$$
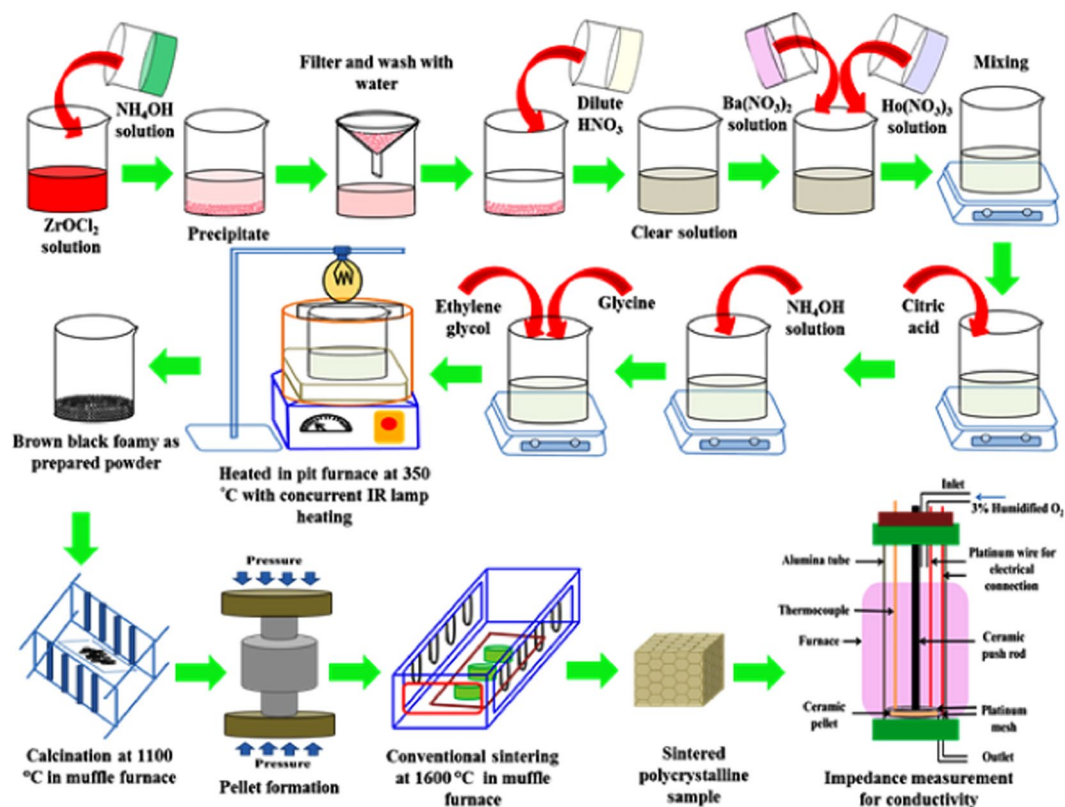
Figure 8. Schematic of processing of Ho-substituted $BaZrO_3$ ceramic by a flash pyrolysis process followed by a conventional sintering, and the obtained conductivity through impedance measurement.

Conclusions

The highly pure and Ho-substituted $BaZrO_3$ nano-sized powders were synthesized through a flash pyrolysis process and followed by conventional sintering. The Rietveld refined XRD pattern approves that all Ho-substituted $BaZrO_3$ samples sintered at 1600 °C revealing $Pm\overline{3}m$ space group of cubic crystal system. The densification and average grain size of all samples are initiated to decrease with the increase of Ho-substitution in $BaZrO_3$ ceramics. This is mainly because of the lower diffusion rate of cation as Ho-substitution in $BaZrO_3$ ceramics increases. Furthermore, the samples exhibit non-uniform electrical microstructure in all probing range of temperature and frequency. The electrical microstructure from grain (bulk) interior and grain boundary is detected from $100\,Hz$ - $1\,MHz$ frequency range for different temperatures. Complex impedance spectra from Nyquist plots reveal that the effect of grain boundary dominates in all over the samples, which is due to the formation of the potential barrier. The total conductivity is increased with the intensification of substitution of Ho-content in $BaZrO_3$ ceramics. This is because of the creation of additional oxygen vacancies. The total estimated electrical conductivity of $BaZr_{0.8}Ho_{0.2}O_{3-\delta}$ sample has arrived to be 5.8×10^{-3} S-cm^{-1} at 600 °C. Therefore, flash pyrolysis route is a most robust technique to synthesize highly pure and nano-sized $BaZr_{1-x}Ho_xO_{3-\delta}$ ($x = 0.05, 0.10, 0.15,$ and 0.20) ceramics powder, which may be assisted to improve the electrical conductivity of electrolyte ceramics for SOFCs.

Methods

Chemicals. Unless otherwise stated, nano-sized $BaZr_{1-x}Ho_xO_{3-\delta}$ ($x = 0.05, 0.10, 0.15$ and 0.20) powders were prepared by flash pyrolysis method using high purity (>99%) raw materials: $Ba(NO_3)_2$, $ZrOCl_2.8H_2O$, $Ho(NO_3)_3.5H_2O$ (Alfa Aesar).

Powder preparation. At first, $ZrOCl_2.8H_2O$ was added in deionized water, and then, it was precipitated as hydrated hydroxides after addition of liquor NH_4OH. The precipitate was washed repeatedly with deionized water to remove chloride ions. After that, the resultant precipitate was dissolved in dilute HNO_3 solution. A clear aqueous solution of $Ba(NO_3)_2$ and $Ho(NO_3)_3.5H_2O$ was prepared by adding distilled water in required proportion. The stoichiometric amount of aqueous solutions was mixed in 2000 mL beaker using a magnetic stirrer, and the desired amount of citric acid was added to metal ions in the above solution. The ratio of citric acid and metal ions was maintained as 1.5:1 proportion. The pH of the above solution was adjusted at 7 using dilute NH_4OH solution. Furthermore, the calculated amount of glycine (metal ions: glycine = 1:0.5) and ethylene glycol (metal ions: ethylene glycol = 1:1.5) were also added to it. Initially, the citric acid and glycine are played a role of chelating agents, and finally, both are functioned as a fuel during the combustion. The resultant solution was placed in a pit furnace at 350 °C with concurrent IR heating from the top. The water was slowly evaporated, leading to form a gel. Finally, the gel was changed into a low-density black fluffy mass because of sudden combustion in the gel.

To derive Ho-substituted BaZrO$_3$ ceramics in the form of nano-sized particles, as-prepared powder containing carbon and other organic impurity obtained from flash pyrolysis route was calcined at 1100 °C in the alumina crucible for 4 h in air. During heating, the organic part present in as-prepared powder was burnt out in the air to form a nano-sized powders. The quality and formation of the phase of ceramic materials were checked by the XRD pattern.

Preparation of bulk sample. The BaZr$_{1-x}$Ho$_x$O$_{3-\delta}$ (BZH) powders calcined at 1100 °C for 4 h were crushed to obtain very fine powder using agate mortar and pestle for 15 min. The binder solution {(polyvinyl alcohol (PVA)} was mixed in crushed powder to obtain better compactness among granules of the materials and pressed uniaxially in a steel die under the pressure of 340 MPa for 1 min in a hydraulic press. After attaining the pellet form of Ho-substituted BaZrO$_3$ perovskite powder using a hydraulic press, it is still required to densify compacted powder samples (green bodies) with continuous 3D structure. The green pellets of BaZr$_{1-x}$Ho$_x$O$_{3-\delta}$ were sintered at 1600 °C. But, as the evaporation of Ba occurs at such high temperature, the green pellets were hence covered with 10% extra of BaO during sintering to compensate evaporation of Ba from the bulk of pellet. All green pellets were sintered at 1600 °C for sintering time of 8 h. Schematic of processing for Ho-substituted BaZrO$_3$ ceramics by a flash pyrolysis technique followed by a conventional sintering, and the obtained conductivity through an impedance measurement are shown in Figure 8. The sintering was carried out to get dense pellets for proton-conducting electrolyte in SOFCs application. The sintering profile is also displayed in Figure S5.

Material characterization. The X-ray diffraction (XRD) (Bruker D8 Advance) was employed to investigate the information regarding phase and structure features of all samples. The XRD patterns of all samples were recorded within the range of 20° to 120° with a step size of 0.019° and a scan rate of 0.064°/min. Furthermore, High-resolution transmission electron microscopy (HRTEM) (JEOL-JEM-2100) was employed to study the particle size, particle morphology, lattice plane, etc. of the powder calcined at 1100 °C for 4 h. The microstructure features (i.e. grain size, grain morphology, etc.) were investigated through Field emission scanning electron microscopy (FESEM) of Zeiss (Merlin-Gemini II). The distributions of grain size were estimated through ImageJ software for all the samples. The Raman spectroscopic measurement of all sintered samples at 1600 °C was carried out using double pre-monochromator (1800 grooves/mm grating) of Raman spectrophotometer (T64000, Horiba Jobin Yvon Ltd. USA) with 514.5 nm radiation of Ar$^+$ laser.

Electrical impedance measurements. To investigate the total electrical conductivity, a complex plane AC impedance spectroscopic study through a Frequency Response Analyzer (ModuLab, Solartron, UK) from 100 Hz to 1 MHz range was employed. For above measurement, platinum paste (Metalo) was painted for the electrode on both the polished surface (by SiC polishing paper) of circular pellets (diameter: 8 mm, and thickness: 1–2 mm) and followed by heating at 1000 °C for 2 h in the air to prepare as Pt-BaZr$_{1-x}$Ho$_x$O$_{3-\delta}$-Pt symmetric cell configuration. The AC amplitude was set at 300 mV and measurements were carried out in between 300 °C and 800 °C under 3% humidified O$_2$ atmosphere.

References

1. Iwahara, H., Esaka, T., Uchida, H. & Maeda, N. Proton conduction in sintered oxides and its application to steam electrolysis for hydrogen production. *Solid State Ionics.* **3**, 359–363 (1981).
2. Iwahara, H., Uchida, H., Ono, K. & Ogaki, K. Proton conduction in sintered oxides based on BaCeO3. *J. Electrochem. Soc.* **135**, 529–533 (1988).
3. Iwahara, H., Yajima, T., Hibino, T., Ozaki, K. & Suzuki, H. Protonic conduction in calcium, strontium and barium zirconates. *Solid State Ionics.* **61**, 65–69 (1993).
4. Iwahara, H. Proton conducting ceramics and their applications. *Solid State Ionics.* **86**, 9–15 (1996).
5. Bonanos, N. Oxide-based protonic conductors: Point defects and transport properties. *Solid State Ionics.* **145**, 265–274 (2001).
6. Kochetova, N., Animitsa, I., Medvedev, D., Demin, A. & Tsiakaras, P. Recent activity in the development of proton-conducting oxides for high-temperature applications. *RSC Adv.* **6**, 73222–73268 (2016).
7. Medvedev, D., Brouzgou, A., Demin, A. & Tsiakaras, P. Proton-conducting electrolytes for solid oxide fuel cell applications. In advances in medium and high temperature solid oxide fuel cell technology. Springer International Publishing. 77–118 (2017).
8. Katahira, K., Kohchi, Y., Shimura, T. & Iwahara, H. Protonic conduction in Zr-substituted BaCeO3. *Solid State Ionics.* **138**, 91–98 (2000).
9. Bohn, H. G. & Schober, T. Electrical conductivity of the high-temperature proton conductor BaZr0.9Y0.1O2.95. *J. Am. Ceram. Soc.* **83**, 768–772 (2000).
10. Flint, S. D. & Slade, R. C. Comparison of calcium-doped barium cerate solid electrolytes prepared by different routes. *Solid State Ionics.* **77**, 215–221 (1995).
11. Pechini, M. P. & Adams, N. *US pat.* **3**(330), 697 (1967).
12. Chick, L. A. *et al.* Glycine-nitrate combustion synthesis of oxide ceramic powders. *Mater. Lett.* **10**, 6–12 (1990).
13. Jacquin, M., Jing, Y., Taillades, G., Jones, D. J. & Roziere, J. Flash combustion synthesis and characterisation of nanosized proton conducting yttria-doped barium cerate. *J. New Mater. Electrochem. Sys.* **10**, 243–248 (2007).
14. Veith, M. *et al.* Sol-gel synthesis of nano-scaled BaTiO$_3$, BaZrO$_3$ and BaTi$_{0.5}$Zr$_{0.5}$O$_3$ oxides via single-source alkoxide precursors and semi-alkoxide routes. *J. Sol-Gel Sci. Tech.* **17**, 145–158 (2000).
15. Phulé, P. P. & Grundy, D. C. Pathways for the low temperature synthesis of nano-sized crystalline barium zirconate. *Mater. Sci. Eng. B.* **23**, 29–35 (1994).
16. Magrez, A. & Schober, T. Preparation, sintering, and water incorporation of proton conducting Ba$_{0.99}$Zr$_{0.8}$Y$_{0.2}$O$_{3-\delta}$: Comparison between three different synthesis techniques. *Solid State Ionics.* **175**, 585–588 (2004).
17. Descemond, M. *et al.* Characteristics and sintering behaviour of 3 mol% Y$_2$O$_3$.ZrO$_2$ powders synthesized by reaction in molten salts. *J. Mater. Sci.* **28**, 2283–2288 (1993).

18. Liu, S. F. & Fu, W. T. Synthesis of superconducting $Ba_{1-x}K_xBiO_3$ by a modified molten salt process. *Mater. Res. Bull.* **36**, 1505–1512 (2001).
19. Kolen'ko, Y. V., Burukhin, A. A., Churagulov, B. R., Oleinikov, N. N. & Vanetsev, A. S. On the possibility of preparing fine-particle barium zirconate by hydrothermal synthesis. *Inorg. Mater.* **38**, 252–255 (2002).
20. Piticescu, R. M., Piticescu, R. R., Taloi, D. & Badilita, V. Hydrothermal synthesis of ceramic nanomaterials for functional applications. *Nanotechnology.* **14**, 312 (2003).
21. Cai, J. *et al.* Preparation method and cation dopant effects on the particle size and properties of $BaCeO_3$ perovskites. *J. Am. Ceram. Soc.* **88**, 2729–2735 (2005).
22. Rhodes, W. H. Agglomerate and particle size effects on sintering yttria-stabilized zirconia. *J. Am. Ceram. Soc.* **64**, 19–22 (1981).
23. Björketun, M. E., Sundell, P. G. & Wahnström, G. Effect of acceptor dopants on the proton mobility in $BaZrO_3$: A density functional investigation. *Phys. Rev. B.* **76**, 054307-1–054307-9 (2007).
24. Geneste, G. & Dezanneau, G. Competition between elastic and chemical effects in the doping, defect association, and hydration of barium stannate. *Solid State Ionics.* **308**, 121–132 (2017).
25. Imashuku, S. *et al.* Improvement of grain-boundary conductivity of trivalent cation-doped barium zirconate sintered at 1600 °C by co-doping scandium and yttrium. *J. Electrochem. Soc.* **155**, B581–B586 (2008).
26. Gilardi, E. *et al.* Effect of dopant-host ionic radii mismatch on acceptor-doped barium zirconate microstructure and proton conductivity. *J. Phys. Chem. C.* **121**, 9739–9747 (2017).
27. Snijkers, F. M., Buekenhoudt, A., Cooymans, J. & Luyten, J. J. Proton conductivity and phase composition in $BaZr_{0.9}Y_{0.1}O_{3-\delta}$. *Scr. Mater.* **50**, 655–659 (2004).
28. Wang, W. & Virkar, A. V. Ionic and electron-hole conduction in $BaZr_{0.93}Y_{0.07}O_{3-\delta}$ by 4-probe dc measurements. *J. Power Sources.* **142**, 1–9 (2005).
29. Slade, R. C., Flint, S. D. & Singh, N. Investigation of protonic conduction in Yb-and Y-doped barium zirconates. *Solid State Ionics.* **82**, 135–141 (1995).
30. Kreuer, K. D. Aspects of the formation and mobility of protonic charge carriers and the stability of perovskite-type oxides. *Solid State Ionics.* **125**, 285–302 (1999).
31. Han, D., Nose, Y., Shinoda, K. & Uda, T. Site selectivity of dopants in $BaZr_{1-y}MyO_{3-\delta}$ (M = Sc, Y, Sm, Eu, Dy) and measurement of their water contents and conductivities. *Solid State Ionics.* **213**, 2–7 (2012).
32. Ahmed, I. *et al.* Structural study and proton conductivity in Yb-doped $BaZrO_3$. *Solid State Ionics.* **178**, 515–520 (2007).
33. Ahmed, I. *et al.* Synthesis and structural characterization of perovskite type proton conducting $BaZr_{1-x}In_xO_{3-\delta}$ ($0.0 \leq x \leq 0.75$). *Solid State Ionics.* **177**, 1395–1403 (2006).
34. Imashuku, S. *et al.* Dependence of dopant cations on microstructure and proton conductivity of barium zirconate. *J. Electrochem. Soc.* **156**, B1–B8 (2009).
35. Saini, D. S., Singh, L. K. & Bhattacharya, D. Synthesis and electrical characterization of $BaZr_{0.9}Ho_{0.1}O_{3-\delta}$ electrolyte ceramic for IT–SOFCs. *AIP Conf. Proc.* **1942**, 140064-1–140064-4 (2018).
36. Saini, D. S. *et al.* Improved conductivity of spark plasma sintered Ho-substituted $BaZrO_3$ electrolyte ceramics for IT-SOFCs. *Appl. Energy Mater.* **1**, 3469–3478 (2018).
37. Saini, D. S. & Bhattacharya, D. Electrical properties of $BaZrO_3$ ceramic synthesized by flash pyrolysis process. *AIP Conf. Proc.* **1724**, 020104-1–020104-4 (2016).
38. Yamazaki, Y., Hernandez-Sanchez, R. & Haile, S. M. Cation non-stoichiometry in yttrium-doped barium zirconate: Phase behavior, microstructure, and proton conductivity. *J. Mater. Chem.* **20**, 8158–8166 (2010).
39. Kang, S. J. L. Sintering: Densification, grain growth and microstructure. Butterworth-Heinemann. (2004).
40. Schaufele, R. F. & Weber, M. J. First and second-order raman scattering of $SrTiO_3$. *J. Chem. Phys.* **46**, 2859–2861 (1967).
41. Charrier-Cougoulic, I., Pagnier, T. & Lucazeau, G. Raman spectroscopy of perovskite-type $BaCexZr_{1-x}O_3$ ($0 \leq x \leq 1$). *J. Solid State Chem.* **142**, 220–227 (1999).
42. Karlsson, M. *et al.* Short-range structure of proton-conducting perovskite $BaInxZr_{1-x}O_{3-x/2}$ (x = 0 − 0.75). *Chem. Mater.* **20**, 3480–3486 (2008).
43. Slodczyk, A., Colomban, P., Willemin, S., Lacroix, O. & Sala, B. Indirect raman identification of the proton insertion in the high-temperature [Ba/Sr][Zr/Ti]$O_{3-\delta}$ modified Perovskite Protonic Conductors. *J. Raman Spectro.* **40**, 513–521 (2009).
44. Slodczyk, A. *et al.* Substitution and proton doping effect on $SrZrO_3$ behaviour: High-pressure raman study. *J. Raman Spectro.* **42**, 2089–2099 (2011).
45. Gonçalves, M. D., Maram, P. S., Muccillo, R. & Navrotsky, A. Enthalpy of formation and thermodynamic insights into yttrium doped $BaZrO_3$. *J. Mater. Chem. A* **2**, 17840–17847 (2014).
46. Saini, D. S. *et al.* Impedance and modulus spectroscopic analysis of single phase $BaZrO_3$ ceramic for SOFC application. *Ionics.* **24**, 1161–1171 (2018).
47. West, A. R., Sinclair, D. C. & Hirose, N. Characterization of electrical materials, especially ferroelectrics, by impedance spectroscopy. *J. Electroceram.* **1**, 65–71 (1997).
48. Barsoukov, E. & Macdonald, J. R. Impedance spectroscopy: theory, experiment, and applications. John Wiley & Sons (2005).
49. Kingery, W. D. Plausible concepts necessary and sufficient for interpretation of ceramic grain-boundary phenomena: II, solute segregation, grain-boundary diffusion, and general discussion. *J. Am. Ceram. Soc.* **57**, 74–83 (1974).
50. Wynblatt, P., Rohrer, G. S. & Papillon, F. Grain boundary segregation in oxide ceramics. *J. Euro. Ceram. Soc.* **23**, 2841–2848 (2003).
51. Raymond, O., Font, R., Suárez-Almodovar, N., Portelles, J. & Siqueiros, J. M. Frequency-temperature response of ferroelectromagnetic $Pb(Fe_{1/2}Nb_{1/2})O_3$ ceramics obtained by different precursors. Part II. Impedance spectroscopy characterization. *J. Appl. Phys.* **97**, 084108 (2005).
52. Haile, S. M., Staneff, G. & Ryu, K. H. Non-stoichiometry, grain boundary transport and chemical stability of proton conducting perovskites. *J. Mat. Sci.* **36**, 1149–1160 (2001).
53. Cherry, M., Islam, M. S., Gale, J. D. & Catlow, C. R. A. Computational studies of protons in perovskite-structured oxides. *J. Phys. Chem.* **99**, 14614–14618 (1995).
54. Münch, W., Seifert, G., Kreuer, K. D. & Maier, J. A Quantum molecular dynamics study of the cubic phase of $BaTiO_3$ and $BaZrO_3$. *Solid State Ionics.* **97**, 39–44 (1997).
55. Jena, H., Kutty, K. G. & Kutty, T. R. N. Proton transport and structural relations in hydroxyl-bearing $BaTiO_3$ and its doped compositions synthesized by wet-chemical methods. *Mater. Res. Bull.* **39**, 489–511 (2004).
56. Islam, Q. A., Nag, S. & Basu, R. N. Electrical properties of Tb-doped barium cerate. *Ceram. Int.* **39**, 6433–6440 (2013).
57. Kjølseth, C. *et al.* Space-charge theory applied to the grain boundary impedance of proton conducting $BaZr_{0.9}Y_{0.1}O_{3-\delta}$. *Solid State Ionics.* **181**, 268–275 (2010).
58. Han, D., Hatada, N. & Uda, T. Microstructure, proton concentration and proton conductivity of barium zirconate doped with Ho, Er, Tm and Yb. *J. Electrochem. Soc.* **163**, F470–F476 (2016).
59. Sharovaz, N. V. & Gorelov, V. P. Electroconduction and the nature of ionic transport in $BaZr_{0.95}Nd_{0.05}O_{3-\delta}$. Russ. *J. of Electrochem.* **41**, 1130–1134 (2005).

Author contributions

D.S.S. & D.B. conceived and supervised the study. S.T. helped to synthesis nano-particles. A.K. and S.K.S. analyzed characterization data. A.G. and N.K. analyzed impedance data. D.S.S. and A.G. drafted the manuscript. S.M. helped to improve the revised manuscript. All the authors commented on the results, provided ideas for the study, and reviewed the manuscript.

Competing interests

The authors declare no competing interests.

Additional information

Supplementary information is available for this paper at https://doi.org/10.1038/s41598-020-60174-4.

Correspondence and requests for materials should be addressed to D.S.S.

Reprints and permissions information is available at www.nature.com/reprints.

Publisher's note Springer Nature remains neutral with regard to jurisdictional claims in published maps and institutional affiliations.